Water-assisted multistep MOCVD for wafer-scale layer-by-layer growth of WSe_2

Yibing Wang, Songyao Tang, Zhaodong Wang, Yingfang Ding, Hleb Fiadziushkin, Amir Ghiami, Susanne Hoffmann-Eifert, Michael Heuken, Andrei Vescan, and Holger Kalisch*

Received: 23 January 2025 / Revised: 30 April 2025 / Accepted: 27 May 2025 / Published online: 28 August 2025

Thin films and heterostructures of two-dimensional transition-metal dichalcogenides (TMDCs) are attractive due to their unique physical properties. However, during metal–organic chemical vapor deposition (MOCVD), the formation of parasitic bilayers (BLs) before monolayer (ML) coalescence is challenging. In this study, a novel multistep MOCVD process, including the additive H_2O is developed. The aim is to minimize parasitic BL nucleation on WSe_2 ML domains and to grow coalesced uniform ML samples on sapphire substrates. Even after optimization, without additives, BL coverage is approximately 15 percent. We show that introducing H_2O reduces this value to about 2 percent. H_2O is equally effective to restrain parasitic (i.e., premature) nucleation in multilayer WSe_2. Raman, photoluminescence, and x-ray photoelectron spectroscopy measurements neither show oxide species due to H_2O introduction nor any compromise to the structural or optical properties. Our results provide a solid step toward the direct MOCVD of high-quality TMDC multilayers and heterostructures.

Impact statement

Uniform transition-metal dichalcogenide (TMDC) films of controlled thickness (i.e., layer number), and their heterostructures, potentially integrated with other two-dimensional (2D) or three-dimensional/bulk materials, promise significant progress in a wide range of applications covering beyond-CMOS electronics, optoelectronics and even neuromorphic components for next-generation artificial intelligence systems. However, for their commercialization, an industrially mature deposition technology with proven scalability, homogeneity and reproducibility is a major prerequisite. In compound semiconductor technology, metal–organic chemical vapor deposition (MOCVD) is the leading technique satisfying all of these requirements. MOCVD is also well suited to grow TMDC films of high quality, but still, quite little is known about the underlying microscopic processes of film formation. Especially, limited migration lengths of metal adatoms cause premature secondary nucleation which manifests in, for example, parasitic bilayer formation on monolayer domains and nonplanarity in 2D-2D heterostructures. In theory, microscopic processes between initial precursor decomposition and final film formation can be tuned by additives to mitigate this problem. However, just a few publications exist, and to the authors' knowledge, none about the introduction of H_2O to TMDC MOCVD processes. In this study, the effects of H_2O addition to a previously optimized WSe_2 growth process are studied, and its impact on migration length are elaborated.

Introduction

With the increased exploration of transition-metal dichalcogenide (TMDC) compounds of the (W, Mo)(S, $Se)_2$ group, a wide range of applications for these materials have been proposed. Especially TMDC heterostructures have captivated the attention of numerous scientists, owing to unique characteristics, suitable for applications in electronics, optics, and various other fields.[1–6] Heterostructures are prepared either by mechanically stacking monolayers (MLs) via transfer or directly through seamless layer-by-layer deposition. In general, two-dimensional (2D) MLs can be mechanically exfoliated from bulk crystals, or a deposited TMDC ML can be peeled off from its substrate by transfer methods.[7] Wafer-scale TMDC heterostructures with a very high uniformity and clean interface can be achieved through advanced transfer techniques, and outstanding performance of devices based on such vertically stacked heterostructures has been demonstrated.[8] However, these methods are time-consuming and have a relatively low yield and reproducibility. Furthermore, structural damage and impurities from the

Yibing Wang, Compound Semiconductor Technology, RWTH Aachen University, Aachen, Germany; wang@cst.rwth-aachen.de
Songyao Tang, Compound Semiconductor Technology, RWTH Aachen University, Aachen, Germany; tang@cst.rwth-aachen.de
Zhaodong Wang, Peter-Grünberg-Institute, Forschungszentrum Jülich GmbH, Jülich, Germany; zh.wang@fz-juelich.de
Yingfang Ding, Compound Semiconductor Technology, RWTH Aachen University, Aachen, Germany; ding@cst.rwth-aachen.de
Hleb Fiadziushkin, Compound Semiconductor Technology, RWTH Aachen University, Aachen, Germany; fiadziushkin@cst.rwth-aachen.de
Amir Ghiami, Compound Semiconductor Technology, RWTH Aachen University, Aachen, Germany; ghiami@cst.rwth-aachen.de
Susanne Hoffmann-Eifert, Peter-Grünberg-Institute, Forschungszentrum Jülich GmbH, Jülich, Germany; su.hoffmann@fz-juelich.de
Michael Heuken, Compound Semiconductor Technology, RWTH Aachen University, Aachen, Germany; AIXTRON SE, Herzogenrath, Germany; m.heuken@aixtron.com
Andrei Vescan, Compound Semiconductor Technology, RWTH Aachen University, Aachen, Germany; vescan@cst.rwth-aachen.de
Holger Kalisch, Compound Semiconductor Technology, RWTH Aachen University, Aachen, Germany; kalisch@cst.rwth-aachen.de
*Corresponding author
doi:10.1557/s43577-025-00948-1

transfer processes are expected to impact heterostructure purity, interlayer coupling, and the performance of fabricated devices.[9,10] Direct synthesis, employing techniques such as metal—organic chemical vapor deposition (MOCVD), has emerged as the most promising method for preparing TMDC heterostructures due to superior interface cleanliness, high reproducibility, and inherent scalability.[11–13] However, the deposition of TMDC heterostructures using MOCVD commonly does not yield layer-by-layer grown heterostructures. Typically, parasitic bilayer (BL) nuclei form on the ML before the ML itself has coalesced, leading to significant deviations from planarity. Even more concerning, such nuclei on the first ML preferably serve as growth sites during subsequent deposition. This process leads to increasing corrugation and nonplanarity with each deposited layer. Therefore, diminishing premature BL nucleation is one of the key challenges for the direct synthesis of heterostructures by MOCVD. In recent years, many strategies on reducing the formation of BLs and promoting lateral growth of a ML have been reported.[14–17] As growth of a ML proceeds, domain size and total ML coverage gradually rise, increasing the likelihood of metal atom arrival on TMDC ML domains rather than on the substrate. As the domain sizes increase, atoms adsorbed on ML domains need to travel longer distances to reach the edges. The related characteristic length is termed migration length in a paper published by Tang et al. and found to be 51 ± 2 nm for W under conditions typical for MOCVD with metal–organic S sources.[18] The authors propose to gradually decrease the W precursor flux as the ML domain size increases. This reduces the W adatom concentration along with the partial pressure of W species. In contrast to lateral growth, nucleation is a nonlinear process and requires a critical cluster size to be exceeded.[19] This is becoming less probable with lower W adatom arrival rates, resulting in an increase of the effective migration length.[18] However, even using such ramping-down strategies, the WS_2 BL coverage in this publication remained around 20 percent. With the same intention, Seol et al. implemented a cyclic interruption of metal precursor injection to reduce the adsorption rate of Mo and W adatoms. Unstable MoS_x or WS_x clusters (nuclei smaller than the critical nucleus size) formed on ML domains are disintegrating during the interruptions, and W or Mo species diffuse to the edge of the ML domains.[19] The migration length of the metal adatoms was also improved by this approach. Using additives is another important approach to tune the growth process restraining BL formation in favor of lateral growth. Voronenkov et al. claimed that volatile metal species could be formed through a reversible reaction between metal precursors and additives, such as water, Cl_2, or HCl. Without additives, metal atom adsorption is determined to be a one-way process, which means that metal adatoms do not desorb once physisorbed to the substrate surface.[20] However, if adsorption and desorption rates of metal adatoms would be appropriately balanced, the adatoms could undergo multiple cycles of adsorption, surface diffusion/migration, desorption, and gas-phase

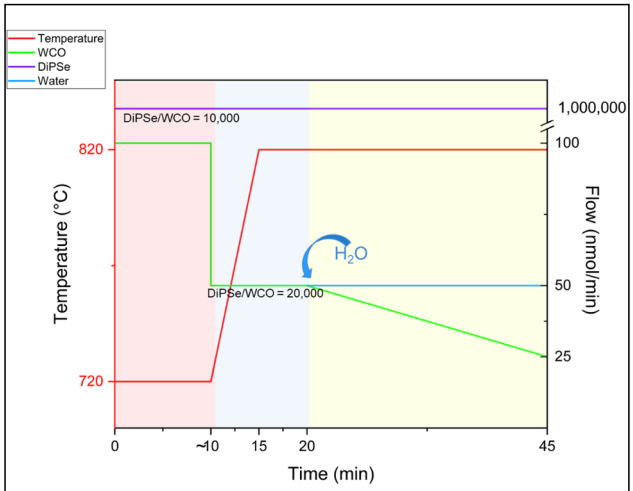

Figure 1. Schematic metal–organic chemical vapor deposition recipe (precursor fluxes and temperature) of monolayer WSe_2. The red, blue, and yellow shaded regions represent nucleation, lateral-growth, and ramping-down stages, respectively. (The molar flows and times shown in this figure represent the actual numbers for samples MS and MS_W.)

diffusion before being incorporated. In this sense, gas-phase diffusion is the key to promote lateral transport of adatoms, increasing the effective migration length, with a suppression of premature BL formation and an enhancement of lateral growth as the consequences.[20] Based on this theory, Groven et al. explored the use of halogen additives, such as HCl and Cl_2, in WS_2 MOCVD. Chlorine-based additives react with W adatoms, rendering the adsorption of W adatoms reversible, and gas-phase diffusion is enhanced.[21] ML WS_2 samples with micrometer-scale domain sizes were successfully achieved on SiO_2 substrates, attributed to a significantly enhanced migration length.[22] However, the typically used halogen-based or alkali-metal additives, such as NaCl, KI,[22,23] HCl, Cl_2[21,24] and sodium propionate,[25] potentially introduce impurities, which deteriorate the performance of devices fabricated subsequently.[26] Furthermore, additives such as HCl and Cl_2 are toxic and corrosive, posing significant safety hazards during the production process.

As an alternative, H_2O,[27,28] a nontoxic and (relatively) noncorrosive additive, is selected in this work to enhance the gas-phase diffusion of metal adatoms and improve layer morphology, in line with the proposal of Voronenkov et al.[20]. As described in that publication, by H_2O addition, an intermediate volatile species such as WH_2O_4 is predicted to form and add a metal desorption—gas-phase diffusion—adsorption path to the microscopic growth processes. In this paper, we report on a multistep water-assisted MOCVD process to prepare WSe_2 MLs with minimal BL nucleation on 2-in. sapphire substrates. As a reference, a multistep MOCVD process based on the previously mentioned publication by Tang et al. with increased migration length of metal atoms by metal ramp-down is selected/designed.[18] As a next step, H_2O is introduced into the chamber as an additive. The impact of H_2O during WSe_2

MOCVD is discussed after characterization of the samples, including a study of the migration length enhancement and an analysis of potential contaminations introduced by the additive H_2O. The use of H_2O as an additive to analogously restrain premature nucleation for thicker layers (BL and tri-layer [TL]) is also discussed at the end.

Methods

All samples of this study were grown in a commercial AIXTRON CCS (close-coupled showerhead) MOCVD reactor in 7 × 2-inch configuration. The reactor is equipped with a pyrometric ARGUS top-side temperature controller (TTC) for temperature homogeneity and *in situ* monochromatic and spectral reflectance monitoring tools. *In situ* reflectance transients allow for a direct *in situ* monitoring of deposition. Two-inch *c*-plane sapphire with a nominal 0.2°–0.25° off-cut toward m-plane is used as substrates for all samples. WCO (tungsten hexacarbonyl, 99.99 percent purity) and DiPSe (di-iso-propyl selenide, 99.999 percent purity) from Dockweiler Chemicals are used as precursors for preparing WSe_2. Ultrapure H_2O (99.9999 percent) from the same manufacturer is employed as an additive during growth. (The MOCVD tool is equipped with two run-lines and CCS plenums, one for chalcogen precursors, the other for metal precursors. H_2O is injected via the same MO run-line and plenum as for WCO.) Purified H_2 is used as carrier gas. The molar precursor and additive fluxes are calculated based on the Antoine equation,[29] which is explained in detail in section S1 of the Supplementary Information.

A standard sapphire desorption procedure at 1050℃ for 30 min under a 150-hPa H_2 atmosphere is applied as the first step for all processes.[30] During growth, the pressure of the MOCVD chamber is reduced to 20 hPa, which minimizes carbon incorporation from the precursors.[18]

A schematic of the basic multistep recipes employed in this work is shown in **Figure** 1. They consist of (1) a nucleation stage at relatively low temperature (i.e., 720℃) for 8–10 min, (2) a lateral-growth stage at higher temperature, and (3) the metal precursor ramping-down stage toward film coalescence. Before nucleation, the temperature is ramped down from 1050℃ (desorption temperature) to the nucleation temperature of 720℃. In the nucleation stage, WCO and DiPSe are introduced into the chamber. A high metal precursor flux combined with a relatively low temperature promotes the formation of stable nuclei with a sufficient density allowing for ML coalescence at the end of the process. The required nucleation density and maximum ML domain size for coalescence are tightly correlated. While a too low nucleation density will trigger BL nucleation before coalescence, a too high density causes an excessive concentration of grain boundaries in the final film. The nucleation stage has to be terminated before secondary nucleation on the ML nuclei is setting on.[18]

During the lateral-growth stage, the WCO flux is initially halved while the temperature is linearly increased to 820℃ over 5 min.[18] Both parameter changes are intended to promote adatom migration/diffusion on the surfaces and increase the critical nucleus size. Their aim is to stop further nucleation in favor of lateral growth of existing domains. After the lateral-growth stage, the ML domains have expanded to a size limited by migration length. In the following metal precursor (WCO) ramping-down stage, the flux of WCO is linearly ramped down over 19 or 25 min while the DiPSe supply is kept constant. Gradually reducing the flux of W effectively increases the migration length of W adatoms, as previously explained. However, considerable BL formation still occurs during the ramping-down stage due to the limited migration length. To investigate the effect of H_2O as an additive, this process is repeated, and H_2O with a flux equal to the WCO value is introduced right at the beginning of the metal precursor ramping-down stage.

As a starting point for our study, the chemical compatibility of H_2O with the other precursors is investigated, along with a preliminary assessment of its impact on WSe_2 growth. For this purpose, samples X1 and X2_W, without and with H_2O, respectively, are grown as simple nucleation-only experiments. Here, the nucleation time was maximally extended to be able to optimally visualize the impact of H_2O in this stage. The subsequent lateral-growth and ramping-down stages are not performed for these samples.

The development and details of water-assisted multistep MOCVD processes are demonstrated in the following discussion with several samples, all listed in Tables I and II (in addition to the initial samples X1 and X2_W). Three N samples (N2, N6 and N10) are analyzed to study nucleation, while samples R_8, R_14, MS, MS_W, and MS_W_A (R, MS, and W represent ramping-down, coalesced ML sample and added water, respectively) are examined to investigate the growth progression toward coalescence and to evaluate the impact of H_2O. SL_N, SL_NL, and SL_NL_W are used to discuss the effect of H_2O on multilayer WSe_2 samples.

To investigate the structural and optical characteristics of the films, scanning electron microscopy (SEM) as well as atomic force microscopy (AFM), photoluminescence (PL), Raman and x-ray photoemission (XPS) spectroscopy are employed. All results presented in this article are based on the central region of the respective samples. In SEM secondary-electron (SE) images (in-lens detector), contrast is influenced by factors such as surface topography, atomic number of materials and electron density. In our experience, these effects cumulate in a darker appearance with a rising height of deposited TMDC on sapphire. The sapphire surface is generally smoother than the deposited TMDC domain, contributing to its excellent SE emission efficiency. As a result, the sapphire surface exhibits a higher SE yield than the TMDC surface, appearing brighter in SEM images.[31] The coverage values of ML, BL, and beyond are calculated using ImageJ based on the average of at least three typical SEM images from the wafer center.[32] The images are first smoothed to minimize background noise, followed by contrast enhancement to improve the differentiation of distinct WSe_2 domains. By setting thresholds, regions with different contrast levels are identified, and their corresponding areas are quantified as percentage values. Samples with over 99 percent

Table I. Detailed summary of growth parameters of WSe_2 samples for developing coalesced monolayer recipes.

ID	X1	X2_W	N2	N6	N10	R_8	R_14	MS	MS_W	MS_W_A
Description			Nucleation samples			Samples with different WCO ramping-down times		Coalesced samples	Coalesced samples with added water	
Nucleation time (min)	100	120	2	6	10	10	10	10	10	10
Nucleation temperature (°C)	780	720	720	720	720	720	720	720	720	720
Lateral-growth time (min)	/	/	/	/	/	10	10	10	10	10
Lateral-growth temperature (°C)	/	/	/	/	/	820	820	820	820	820
Ramping-down time (min)	/	/	/	/	/	8	14	25	25	19
WCO flux (nmol/min) during nucleation/lateral-growth / ramping-down	25/–/–	25/–/–	100/–/–	100/–/–	100/–/–	100/50/50 → 25	100/50/50 → 25	100/50/50 → 25	100/50/50 → 25	100/50/50 → 25
DiPSe flux (µmol/min)	1000	1000	1000	1000	1000	1000	1000	1000	1000	1000
H_2O flux (nmol/min)	/	50	/	/	/	/	/	/	50	
Sapphire offcut (°)	0.25	0.25	0.2	0.2	0.2	0.2	0.2	0.2	0.2	0.25

ML coverage are termed as "fully coalesced." Per definition, ML, BL, TL coverages may sum up to more than 100 percent because, for example, a region identified as BL also contributes to ML coverage (because a ML had been grown before the second molecular sheet is deposited). Raman and PL measurements are conducted using a 532-nm laser with a power of 1 mW. All AFM images are recorded in tapping mode and ambient air. XPS analysis was performed with a monochromatic Al Kα source at 1486.6 eV. To prevent sample charging during measurements, an electron neutralizer emitting a 20-µA current with a bias of 1.37 eV is employed. High-resolution XPS scans are executed with a pass energy of 10 eV and a step size of 0.1 eV. The XPS data of samples W0, W2, W6, and W10 are analyzed to verify whether water either is incorporated into the WSe_2 samples or impacts the chemical bonds via partial oxidation.

Results and discussion

Effect of H_2O addition

Initially, to study the effect of H_2O, especially on the onset of BL nucleation, two samples are prepared. Both samples X1 and X2_W are deposited using a single-step MOCVD process, involving 100 min/120 min of growth with a constant WCO flux of 25 nmol/min and DiPSe flux of 1000 µmol/min at 780℃. High temperature and low metal precursor flux are chosen, targeting a sparse nucleation density resulting in large, isolated domains. Sample X2_W is prepared under identical conditions, with the addition of 50-nmol/min H_2O injection throughout the entire process, and the growth time is extended by 20 min to achieve a large domain size.

The SEM images of the two samples, shown in **Figure 2**, clearly highlight significant differences. As discussed in the "Methods" section, the brightest areas in Figure 2a–b represent the sapphire surface. ML domains feature a darker contrast with the darkest shade corresponding to BLs confined within the ML domains. The size of a triangular WSe_2 domain is defined here as the edge length of the largest triangular domain observed in each SEM image. The mean domain size of sample X2_W with the additive H_2O and an additional 20 min of growth time (~755 ± 43 nm) is significantly larger than that of sample X1 grown without H_2O and with a shorter growth time (~559 ± 22 nm). In Figure 2a, red circles are marking the BL clusters already formed on all ML domains of sample X1. Despite its longer growth time, BL formation is just beginning on some ML domains of sample X2_W (with added H_2O) and is not observed on others (Figure 2b). These results initially demonstrate that H_2O is compatible with our precursor chemistry and effectively reduces BL formation by enhancing the migration length. Further studies on the role of H_2O in the formation of coalesced ML, BL, and TL films will be discussed in the following sections.

Table II. Summary of growth parameters of WSe_2 samples for studying the effect of H_2O on multilayer WSe_2.

ID	W0	W2	W6	W10	SL_N	SL_NL	SL_NL_W
Description	Samples series for XPS				Samples for multi-layer studies		
Nucleation time (min)	10	10	10	10	8	8	8
Nucleation temperature (°C)	720	720	720	720	720	720	720
Lateral-growth time (min) First layer/Second layer	24/–	24/–	24/–	24/–	10/65	10/65	10/65
Lateral-growth temperature (°C)	820	820	820	820	820	820	820
Ramping-down time (min)	/	/	/	/	19	19	19
WCO flux (nmol/min) during nucleation/ lateral-growth /ramping-down	100/50/–	100/50/–	100/50/–	100/50/–	100/50/50→25	100/50/50→25	100/50/50→25
WCO flux for second layer (nmol/min) Nucleation/lateral-growth	/	/	/	/	100/–	100/50	100/50
DiPSe flux (µmol/min)	1000	1000	1000	1000	1000	1000	1000
H_2O flux (nmol/min)	/	100	300	500	50	50	50
H_2O flux for second layer (nmol/min)	/	/	/	/	/	/	50
Sapphire offcut (°)	0.2	0.2	0.2	0.2	0.25	0.25	0.25

Nucleation of WSe_2

The nucleation stage is now optimized to allow for WSe_2 ML coalescence (cf. Figure 1). While the temperature and flow determine the nucleation density, the optimal nucleation time needs to be determined through a series of experiments. Three samples, N2, N6, and N10, correspond to nucleation times of 2, 6, and 10 min, respectively. Details of growth are summarized in Table I.

SEM images of these samples are presented in **Figure** 3a–c. As nucleation time is increased, the domain size and coverage are becoming larger. The domain size gradually rises from ~0.04 to ~0.13 µm, as shown in Figure 3d. The domain shape also evolves, changing from irregular three-point-star-like shapes to triangular. The concave shape of the domain forms when metal adatoms on the sapphire surface accumulate at the corners of the nuclei due to limited diffusion along edges, creating a concave structure.[33] However, as nucleation proceeds, more adatoms arrive on the ML domain area, and these adatoms can overcome the Ehrlich–Schwoebel (E–S) barrier to attach to the edges of the underlying domain and eventually restore its triangular shape.[34–36] The nucleation density of sample N2 is ~120 nuclei/µm^2, whereas those of N6 and N10 are decreased to ~75 and ~80 nuclei/µm^2, respectively. The slightly dropping density between minutes 2 and 6 of nucleation can be attributed to two aspects. First, once a certain number of nuclei have formed on the substrate, the critical adatom concentration required for additional nucleation is no longer reached. Second, when growing in lateral size, adjacent ML nuclei can merge into larger ones (reducing the initial nucleation density). When the nucleation time reaches 10 min (sample N10), small BL nuclei appear on the ML domain, highlighted by red circles in Figure 3c. This indicates that the lateral growth of ML domains without BL nucleation has reached its limit under these growth (i.e., nucleation) conditions. Therefore, a nucleation time of 8–10 min is selected for all subsequent samples.

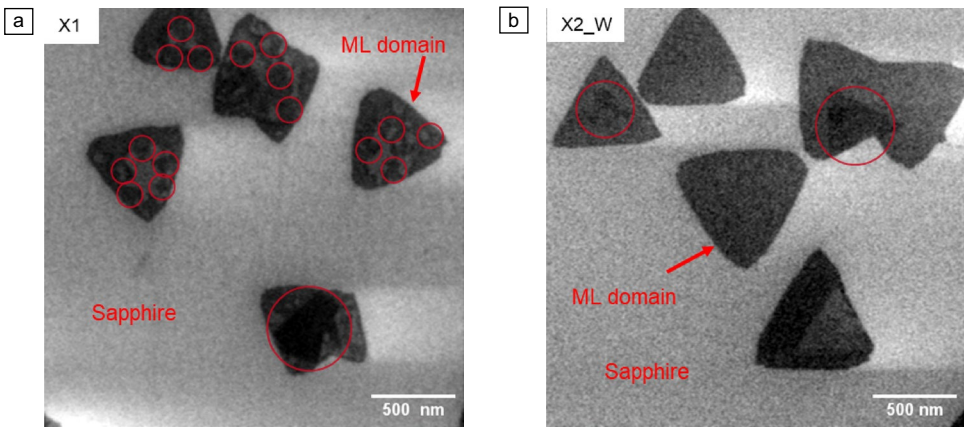

Figure 2. Scanning electron microscopy images of samples X1 (a) and X2_W (b). Bilayer nuclei are encircled in red. ML, monolayer.

Lateral growth and ramping-down stage

Samples MS and MS_W, as already introduced in Figure 1, are grown by a full ML recipe including a 25 min. ramping-down stage for coalescence. In the following, two

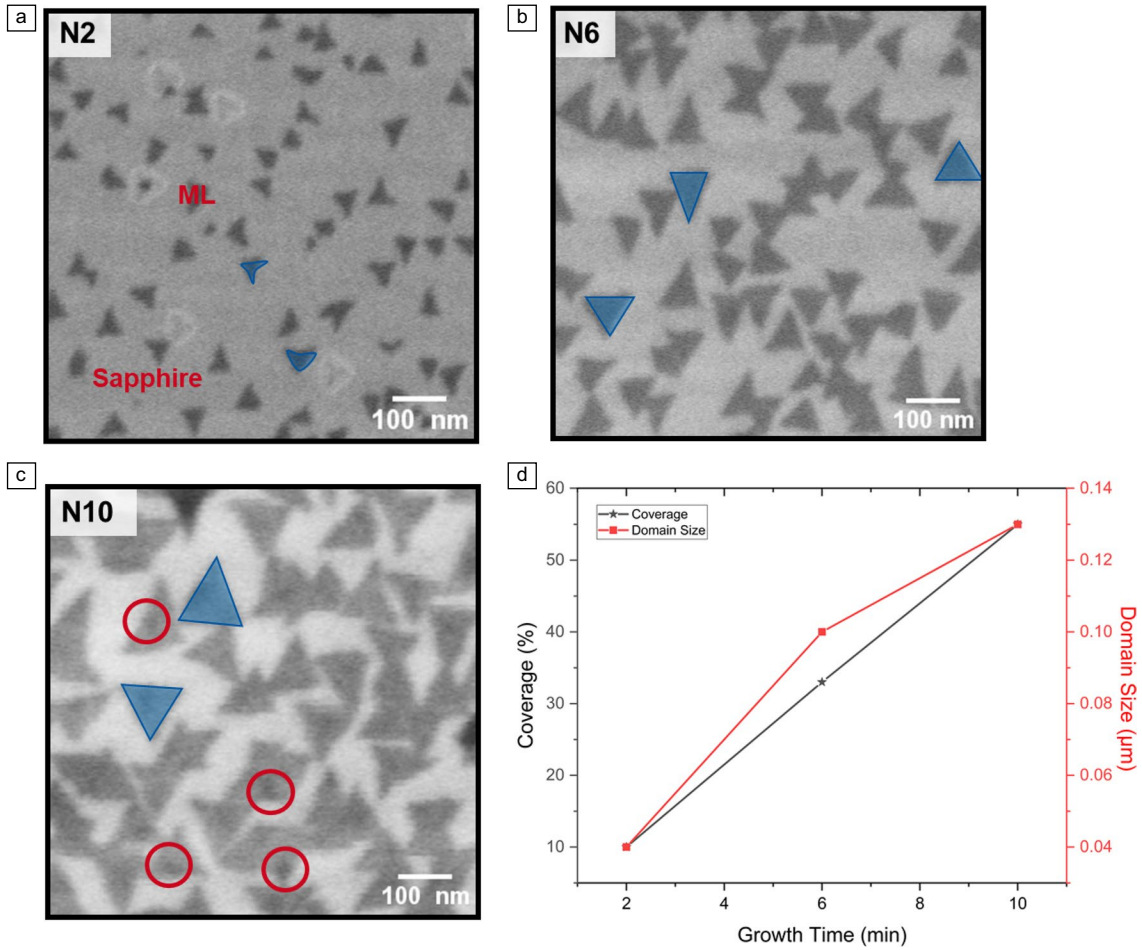

Figure 3. (a–c) Surface morphology of WSe_2 after different nucleation times, ranging from 2 to 10 min (samples N2, N6 and N10). (d) WSe_2 nucleation domain size and coverage as a function of nucleation time. The domain size recorded here is the largest domain size observed with scanning electron microscopy.

samples (R_8 and R_14), obtained by stopping this process after 8 and 14 min of WCO ramping-down (see Figure 1), are characterized and discussed. As summarized in Table I, a reference coalesced sample MS without H_2O addition and a sample MS_W with 50 nmol/min H_2O during the full 25-min ramping-down stage are also studied.

After 8 min of growth in the ramping-down stage, sample R_8 exhibits ~2 percent BL coverage and ~89 percent ML coverage (**Figure** 4a). Accordingly, the bright regions in Figure 4a are uncovered sapphire. In comparison, the ML coverage of sample R_14 with longer ramping-down time shows a minimal increase by ~2 percent. However, its BL coverage roughly triples to ~6 percent. This indicates that instead of contributing to ML coalescence, a rising fraction of newly arrived adatoms fail to migrate to the edges of the existing ML domains, resulting in continuous BL nucleation. The migration length is evidently smaller than the average domain size at a certain point of domain growth. Although the introduction of the ramping-down stage has delayed this critical point, the impact of metal ramping-down on migration length is still insufficient to achieve a fully coalesced WSe_2 sample with minimal BL coverage.

Sample MS was obtained by completing the full recipe with a 25-min ramping-down stage and serves as a reference for water addition. MS is a fully coalesced WSe_2 ML with approximately 15 percent BL coverage, as extracted from the SEM image shown in Figure 4b. The corresponding AFM image confirms the presence of BL domains and even reveals some TL ~ few-layer (FL) regions. From the AFM image in Figure 4b, the step profiles of three characteristic features have been analyzed to better distinguish the different WSe_2 domains. In profile 1 and profile 3, the presence of BL domains is evident, with a measured step height of ~1 nm being consistent with the expected step from WSe_2 ML to BL. Profile 2 captures a more complex layer structure. It initially crosses a small BL region before transitioning into a FL region, followed by a short TL segment, and finally reaching the ML level. Although extended exposure to air has probably led to

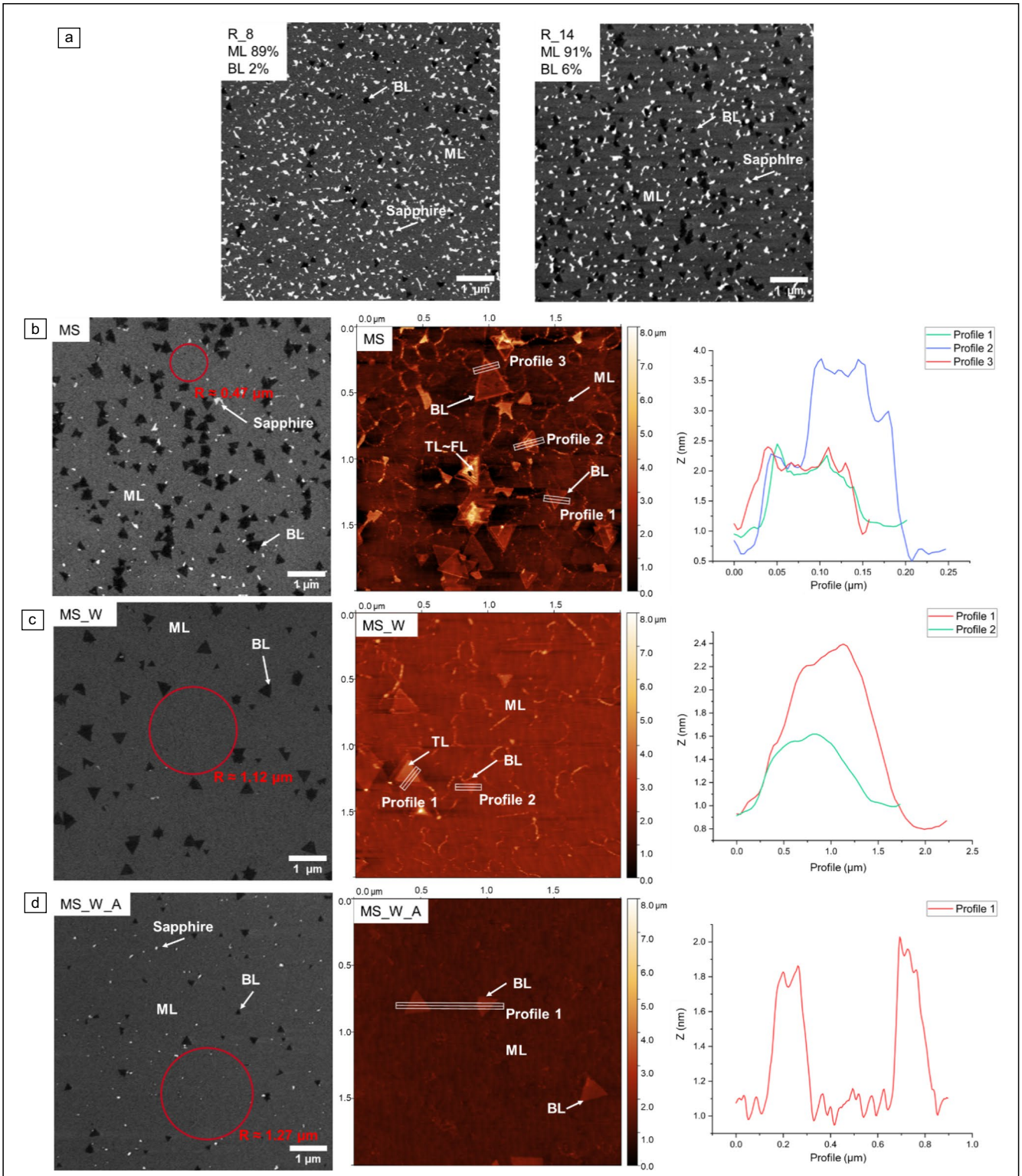

Figure 4. (a) Scanning electron microscopy (SEM) images of samples after stopping growth during WCO ramping-down, R_8 (left) and R_14 (right). Morphology of fully coalesced monolayer (ML) WSe_2 samples MS without H_2O (b) and MS_W with H_2O addition (c). (d) Morphology of sample MS_W_A. The left image is the corresponding SEM image, on which an estimate of nominal migration length is marked by red circles. The middle one is the corresponding atomic force microscopy (AFM) image, and the right ones show extracted AFM step profiles. BL, bilayer; TL, tri-layer; FL, few layer.

height variations at the domain edges compared to the flat inner regions,[37] the layer morphology remains well distinguishable. For sample MS_W, the additive H_2O is introduced during the ramping-down stage at a molar flux equivalent to the initial value of WCO. As shown in the SEM images in Figure 4c, the BL coverage of sample MS_W is significantly reduced from ~15 to ~6 percent. This is further corroborated by the AFM image in Figure 4c, which clearly demonstrates a substantial reduction in BL formation. The corresponding step profile of sample MS_W reveals two characteristic regions, which are consistent with BL and TL domains, respectively.

For both samples MS and MS_W, sapphire defects are also visible in the AFM scans in Figure 4b–c. Especially, some pinholes probably originating from gas bubbles in the sapphire melt [38] are verified by examining sapphire substrates after desorption only (Figure S1). Those defects on the surface of sapphire provide additional nucleation sites, leading to an increase in nucleation density and thus a decrease in the quality of TMDC films.[34] To address this in the following, we have chosen sapphire wafers of (supposedly) higher quality. These wafers have a slightly different offcut of 0.25° and appear to have a lower defect density. For these substrates, minor adjustments to the growth recipe are necessary to account for the subtle 0.05° offcut difference and the improved surface quality. To ensure consistent nucleation results, the nucleation time is shortened to 8 min. A more detailed comparison of nucleation can be found in S3. As a result, the WSe_2 ML sample MS_W_A with a BL coverage of only ~2 percent is successfully obtained. The SEM image of this sample is shown in Figure 4d. AFM analysis of sample MS_W_A confirms ML WSe_2 with reduced BL coverage and reveals a smoother topography. Its step profile clearly reveals two BL regions, each with a height of approximately 0.8 nm, which is consistent with the thickness of a ML WSe_2.

The effect of H_2O is also confirmed by *in situ* reflectance measurements (**Figure** 5). Here, the 405-nm reflectance trace and its slope as functions of growth time for the two samples MS and MS_W are plotted. It is widely accepted that there is an approximately linear relationship between the reflectance slope and the deposition rate.[18,39] During the nucleation stage (0–10 min) for both samples, the reflectance increases strongly with growth time. The slope curve rises sharply within the first 2 min, but then gradually decelerates between 6 and 10 min. This could be attributed to the difference between the formation of a high density of subcritical nuclei and the extension of existing domains way above the critical nucleus size.[39] During the lateral growth stage (10–20 min), the absolute reflectance increases steadily over time, accompanied by a decreasing slope. This decline is attributed to the reduction of the WCO flux by half and a smaller growth rate caused by the temperature ramp-up. Until the beginning of the ramping-down stage, the reflectance curve of sample MS_W closely overlaps with that of sample MS. However, starting from the ramping-down stage, with H_2O introduced for sample MS_W, the curves of the two samples begin to diverge.

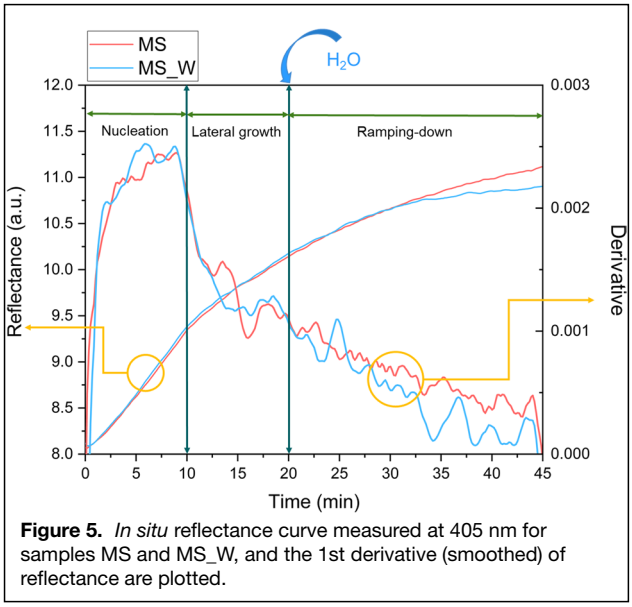

Figure 5. *In situ* reflectance curve measured at 405 nm for samples MS and MS_W, and the 1st derivative (smoothed) of reflectance are plotted.

Compared to sample MS, the slope curve of sample MS_W exhibits a significant reduction, indicating that the growth rate of sample MS_W during this period is lower than that of sample MS. Additionally, the final reflectance of sample MS_W with H_2O is also lower than that of sample MS. This difference is attributed to the diminished BL formation, which also reduces the amount of deposited material. Apparently, adding a gas phase W species by the additive H_2O slightly increases the fraction of desorbed W adatoms which eventually do not contribute to film formation.

The migration length of metal adatoms can be estimated using several methods.[17,40] As the first approach, we apply a method analyzing regions free of BL nuclei on already merged ML domains. The nominal migration length of adatoms is extracted as the radius of the largest circle which can be drawn in such areas (without crossing a BL nucleus, see red circles in Figure 4b–d). The nominal migration length of sample MS_W with added H_2O is ~1.12 µm. This value is more than twice the migration length of W adatom on sample MS without added H_2O (~0.47 µm). The migration length of sample MS_W_A (higher substrate quality) is further increased to ~1.27 µm. Another method determining the effective migration length can be approximated as $\lambda_{M,eff} = \frac{1}{2} \times L_{av}$, where L_{av} is the average distance between nuclei. It can be extracted from the nuclei density N via $L_{av} = \sqrt{\frac{1}{N}}$.[17] A detailed illustration of this calculation can be found in S4. The results consistently indicate that the effective migration length of sample MS_W with added H_2O is ~433 nm, which is again significantly larger than that of sample MS without H_2O (~273 nm). The migration length of the sample MS_W_A is also confirmed to be further increased compared to MS_W to ~583 nm. These results confirm that the additive H_2O effectively enhances the migration of W adatoms, promoting lateral growth and restraining parasitic BL nucleation.

Characterization of WSe_2 films

To characterize the structural and optical properties of samples MS and MS_W (and to reveal possible impacts of H_2O addition), PL and Raman spectroscopy are conducted.

Raman spectra of samples MS and MS_W are shown in **Figure** 6a. The typical characteristics of WSe_2 can be confirmed by the combined $E^1_{2g}+A_{1g}$ (near 250 cm^{-1}) and the 2LA(M) (near 260 cm^{-1}) modes. The additive H_2O does not lead to any significant peak shift or the emergence of additional peaks in Raman spectra. In addition to these two characteristic peaks, a weak signal corresponding to the interlayer breathing mode B (around 309 cm^{-1}) is detected in sample MS without H_2O. The breathing mode is associated with rigid layer shear and is highly sensitive to the presence of BL, even though sample MS possesses only~15 percent BL.[41,42] In contrast, this mode cannot be detected in the MS_W sample with significantly less BL. Carbon-related peaks are not observed in either sample, which indicates a low level of parasitic carbon incorporation. Specific information can be found in S5.

PL spectra of samples MS and MS_W are shown in Figure 6b. Two distinct peaks are identified, labeled as X_E and X_T. X_E corresponds to the emission from A excitons (characteristic for the direct bandgap of ML WSe_2), and X_T is attributed to charged excitons (trions).[43,44] The two main peaks of sample MS (without H_2O) are located at 1.618 eV and 1.659 eV, exhibiting nearly no shift in peak positions compared to the two peaks of sample MS_W with H_2O (1.614 eV and 1.659 eV). This observation confirms that the introduction of H_2O does not lead to significant changes in the band structure within the sample. In addition, the X_E intensity of sample MS_W is higher than that of sample MS, indicating that H_2O reduces the formation of BL (with BL enhancing interlayer coupling and reducing excitonic emission intensity).[42]

To investigate whether the addition of H_2O with higher injection flux affects the chemical properties of WSe_2, samples (W0, W2, W6, and W10) with varying H_2O fluxes are prepared (see Table II) using a recipe that includes only the nucleation and lateral growth stages. H_2O is introduced at the beginning of lateral growth. Compared to the recipe in Table I, the lateral-growth time is extended to 24 min.

The XPS spectra of these samples recorded on the W 4f and Se 3d binding energy regions are shown in **Figure** 7. The peak position of the W 4f doublet (31.1 eV and 33.3 eV) and the Se 3d doublet (53.4 eV and 54.2 eV) are in excellent agreement with the reference of an exfoliated WSe_2 single-crystal flake.[45,46] Even in the sample W10 with the highest flux of H_2O introduced, no detectable peaks associated to codeposited impurities are observed for the W 4f and Se 3d core levels. This suggests that H_2O does not induce notable changes, such as oxidation, in the WSe_2 samples. The XPS data indicate that H_2O primarily affects the growth kinetics without causing doping or altering the oxidation state of W. The stoichiometry of the sample is calculated based on the relative sensitivity factors (RSF) and the peak area corresponding to the main element. For the WSe_2 sample W0 without H_2O, the Se/W stoichiometric ratio is 2.18, while for the sample W10 with the highest amount of H_2O, the ratio is 2.12. The difference lies within the error margin of the measurement (assuming a relative error of about 10 percent). These results indicate that the introduction of H_2O does not significantly affect the stoichiometric ratio of WSe_2 films.

Minimizing TL formation

To verify that the addition of H_2O has a similar effect on the deposition of multilayer WSe_2 (e.g., a BL~TL sample), phases IV and V are added to the optimized ML recipe. Recipe details are displayed in **Figure** 8a.

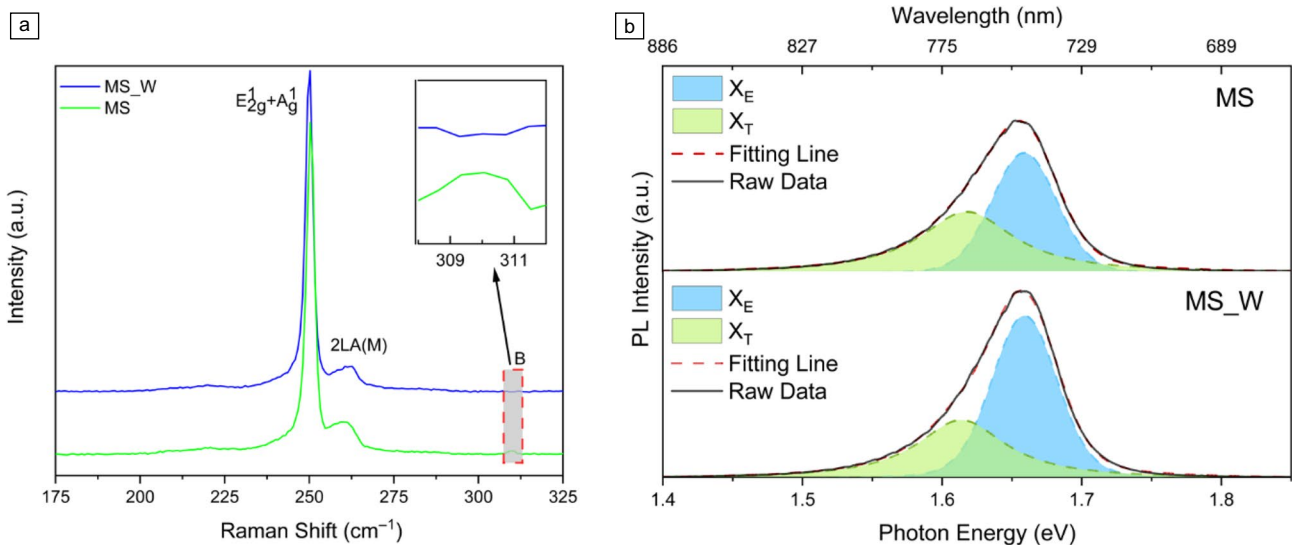

Figure 6. Characterization of WSe_2 films. (a) Raman and (b) Photoluminescence (PL) spectra of samples MS and MS_W.

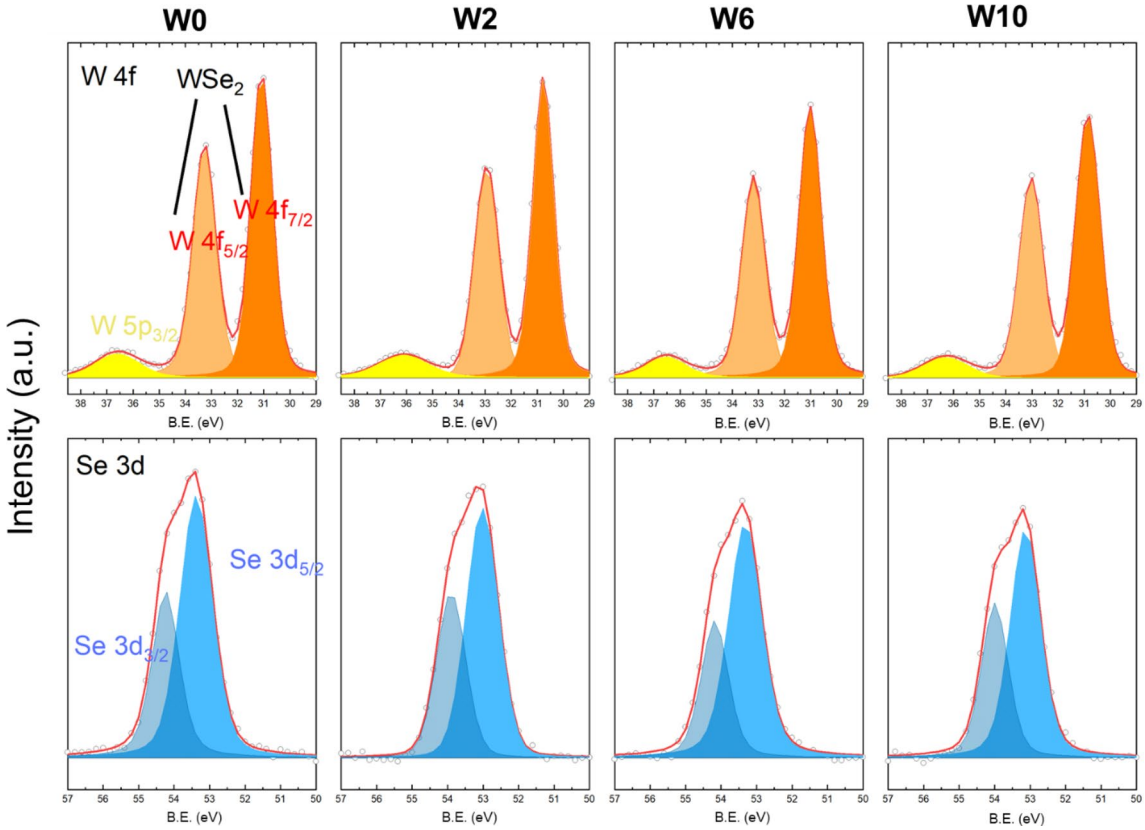

Figure 7. X-ray photoelectron spectroscopy (XPS) spectra (plotted versus binding energy (B.E.)) of W 4f and Se 3d core levels of WSe_2 for samples W0, W2, W6, and W10 with H_2O fluxes of 0×, 2×, 6×, and 10× the WCO flux, respectively.

Phase IV corresponds to the nucleation of the second WSe_2 layer on a coalesced ML, yielding sample SL_N, as shown in the SEM image in Figure 8b. In this sample, a low density of TL nuclei has already formed on the existing BL domains originating from secondary nucleation. Typically, the nucleation density of a BL domain on a ML is lower than that of a ML on sapphire, even with similar growth parameters. As a 2D material, the ML surface possesses a lower density of dangling bonds compared to the sapphire substrate, which results in weaker adsorption and a reduced probability of adatom sticking. Sample SL_NL is obtained by following up the second nucleation stage with a second lateral-growth stage (Phase V). Its surface morphology is shown in Figure 8c. The white area (pointed by green arrow) is the first layer (uncovered ML), whereas the red arrow indicates the contrast of the second layer (uncovered BL). Additionally, the blue arrow (pointing on dark-coloured area) marks the TL region (and even>TL structures). According to calculations by ImageJ, approximately 13 percent of the first layer regions in sample SL_NL remain uncovered. TL and even>TL structures have formed, with the TL coverage being approximately 53 percent. The observation proceeds, during phase V, the second layer of WSe_2 toward BL coalescence, but this is accompanied by the formation of TL domains (and thicker vertically grown domains).

Finally, for sample SL_NL_W, 50 nmol/min H_2O flux is added to support BL growth during phase V. The SEM image of the sample SL_NL_W is shown in Figure 8d. With the addition of H_2O, the BL coverage increases further, reducing the uncovered area to ~9 percent, despite the same amount of precursor used in both deposition processes. The TL coverage also decreases from ~53 to ~48 percent, as expected. These results indicate that the addition of H_2O during the lateral-growth stage also promotes the second WSe_2 layer to grow laterally over the first layer, rather than stacking vertically to form TL or bulk structures. However, further process optimization is still necessary to improve film planarity and realize an ideal layer-by-layer growth of TMDC thin films.

The distribution of TL domain areas for the samples SL_NL and SL_NL_W is summarized in Figure 8e. To accurately determine the statistics of TL domains size, the data shown in Figure 8e exclude domains with areas smaller than 0.15 μm^2 and those larger than 0.45 μm^2 (which have been formed by merging of separate TL domains). In sample SL_NL_W with H_2O, the TL domain areas are primarily between 0.15 and 0.25 μm^2 in size, whereas in sample SL_NL without H_2O, they predominantly range from 0.25 to 0.35 μm^2. This demonstrates that the average TL domain size decreases with the introduction of H_2O, resulting in a greater number of smaller

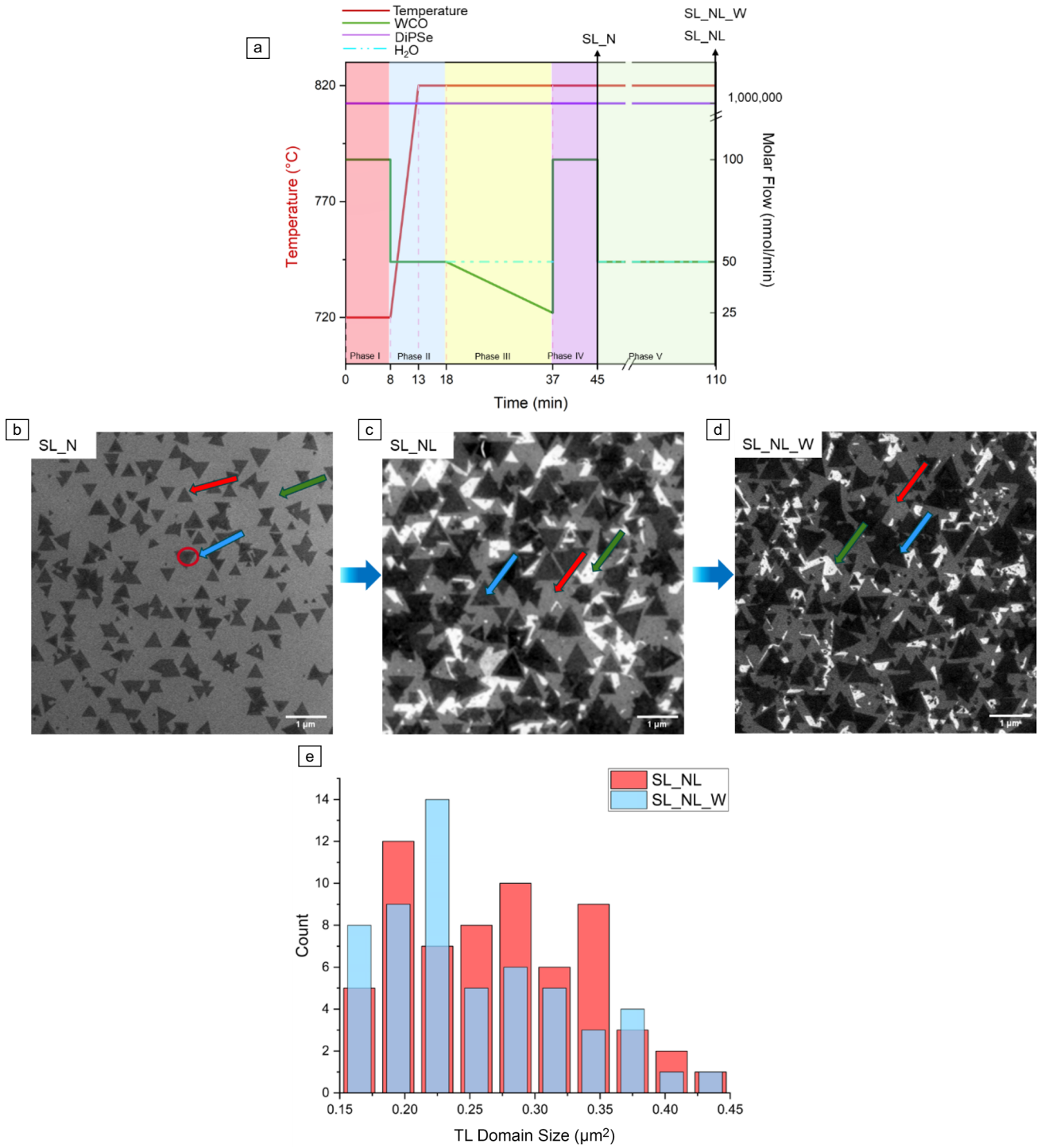

Figure 8. (a) Schematic metal–organic chemical vapor deposition recipe for bilayer (BL) ~ tri-layer (TL) WSe_2 samples SL_N, SL_NL, and SL_NL_W. (b–d) Scanning electron microscopy images of WSe_2 morphology evolution on these samples. Green arrows point to monolayer (ML), red to BL, and blue to TL. (e) Distribution of TL domain size for SL_NL and SL_NL_W.

TL domains compared to sample SL_NL. Rather than incorporating to the already-formed TL domains, adatoms migrate to unfilled second layer regions when the additive H_2O is injected. This process leads to the formation of a larger quantity of smaller TL domains rather than the aggregation into relatively larger TL domains, as observed in SEM images of sample SL_NL without H_2O (Figure 8c). This not only validates our hypothesis that H_2O increases the effective migration

length of adatoms during deposition, but also demonstrates that its effect extends beyond ML samples.

Conclusion

In this work, we developed a multistep MOCVD process with a well-designed ramping-down stage of the W precursor flux to achieve wafer-scale WSe_2 films. This process allows to grow fully coalesced ML WSe_2 samples with low BL formation, initially exhibiting a BL coverage of approximately 15 percent. These films serve as a reference to study the impact of the additive H_2O on WSe_2 growth. The introduction of H_2O as an additive is demonstrated to promote the lateral growth of ML WSe_2 and effectively restrains BL formation through enhanced gas-phase diffusion. With the addition of H_2O, the BL coverage of ML WSe_2 samples is reduced from 15 percent to only ~2 percent. Detailed calculations reveal that H_2O injection increases the migration length of metal adatoms, indicating a direct enhancement in the growth kinetics through facilitated migration. Further characterization, including PL, Raman spectroscopy, and XPS verify that H_2O injection during the deposition process does not significantly impair the structure or chemical properties of the WSe_2 films. Instead, the addition primarily affects growth kinetics, enabling a refined control over film thickness and surface characteristics without inducing defects or altering the intrinsic materials properties. Moreover, our findings demonstrate that H_2O effectively reduces BL and TL growth on fully coalesced ML films, presenting a viable strategy for achieving layer-by-layer growth of TMDCs. The beneficial role of H_2O as an additive in MOCVD is validated in the case of WSe_2 and opens new possibilities for the precisely controlled synthesis of other TMDC materials with similar characteristics. Furthermore, the impact of H_2O-assisted growth on the defect structure of the films (grain boundaries, point defects) as well as on their performance in (opto) electronic devices has to be studied in detail. Future studies will include further methods such as PL spectroscopy at cryogenic temperatures as well as a thorough electrical characterization after field-effect transistor fabrication. In sum, this approach establishes a practical foundation for the direct fabrication of 2D/2D heterostructures via MOCVD. Future work will explore the adaptability of this H_2O-assisted MOCVD technique for a broader range of TMDCs, paving the way for tailored material synthesis with applications in layered heterostructures and novel device architectures.

Author contributions

Y.W. contributed to writing the original draft, investigations, experiment conceptualization, sample preparation as well as data analyses and presentation. S.T. contributed to manuscript review and editing, experiment conceptualization, and sample preparation. Z.W. and S.E. contributed to data collection. Y.D. contributed to sample preparation. A.G. and H.F. contributed to manuscript review and data analysis. M.H. contributed to project coordination. A.V. contributed to manuscript review, supervision, and funding acquisitions. H.K. contributed to manuscript review and editing, experiment conceptualization, supervision, data analyses, and funding acquisitions. All authors actively participated in the scientific discussions.

Funding

Open Access funding enabled and organized by Projekt DEAL. This work was in part funded by the German Research Foundation (DFG, Project No. 414268710 and 461605777), and the Federal Ministry of Education and Research (BMBF, Germany) in the Project NEUROTEC-II (16ME0399 and 16ME0398K) and NeuroSys (03ZU1106AA and 03ZU1106AB).

Data availability

The data generated during the current study are available from the corresponding author on reasonable request.

Conflict of interest

On behalf of all authors, the corresponding author states that there is no conflict of interest.

Supplementary information

The online version contains supplementary material available at https://doi.org/10.1557/s43577-025-00948-1.

Open Access

References

1. K.S. Novoselov, A. Mishchenko, A. Carvalho, A.H. Castro Neto, *Science* **353**(6298), aac9439 (2016)
2. A.K. Geim, I.V. Grigorieva, *Nature* **499**(7459), 419 (2013)
3. A. Piacentini, A. Daus, Z. Wang, M.C. Lemme, D. Neumaier, *Adv. Electron. Mater.* **9**(8), 2300181 (2023)
4. N. Flöry, P. Ma, Y. Salamin, A. Emboras, T. Taniguchi, K. Watanabe, L. Novotny, *Nat. Nanotechnol.* **15**(2), 118 (2020)
5. K.Y. Ko, J.G. Song, Y. Kim, T. Choi, S. Shin, C.W. Lee, H. Kim, *ACS Nano* **10**(10), 9287 (2016)
6. M. Chhowalla, H.S. Shin, G. Eda, L.J. Li, K.P. Loh, H. Zhang, *Nat. Chem.* **5**(4), 263 (2013)
7. C. Kim, M.-A. Yoon, B. Jang, H.-D. Kim, J.-H. Kim, A.T. Hoang, J.-H. Ahn, H.-J. Jung, H.-J. Lee, K.-S. Kim, *NPG Asia Mater* **13**, 44 (2021)
8. K. Kang, K.H. Lee, Y. Han, H. Gao, S. Xie, D.A. Muller, J. Park, *Nature* **550**(7675), 229 (2017)

9. A. Ghiami, T. Sun, H. Fiadziushkin, S. Tang, A. Grundmann, M. Heuken, A. Vescan, *Crystals* (Basel) **13**(10), 1474 (2023)
10. K. Kim, M. Yankowitz, B. Fallahazad, S. Kang, H.C. Movva, S. Huang, E. Tutuc, *Nano Lett.* **16**(3), 1989 (2016)
11. D.H. Lee, Y. Sim, J. Wang, S.-Y. Kwon, *APL Mater.* **8**(3), 030901 (2020). https://doi.org/10.1063/1.5142601
12. D.K. Singh, G. Gupta, *Mater. Adv.* **3**(15), 6142 (2022)
13. S. Cwik, D. Mitoraj, O. Mendoza Reyes, D. Rogalla, D. Peeters, J. Kim, A. Devi, *Adv. Mater. Interfaces* **5**(16), 1800140 (2018)
14. M. Chubarov, T.H. Choudhury, D.R. Hickey, S. Bachu, T. Zhang, A. Sebastian, A. Bansal, H. Zhu, N. Trainor, S. Das, M. Terrones, N. Alem, J.M. Redwing, *ACS Nano* **15**, 2532 (2021)
15. M. Zinke-Allmang, L.C. Feldman, M.H. Grabow, *Surf. Sci. Rep.* **16**(8), 377 (1992)
16. M. Liu, J. Liao, Y. Liu, L. Li, R. Wen, T. Hou, Y. Hao, *Adv. Funct. Mater.* **33**(18), 2212773 (2023)
17. X. Zhang, T.H. Choudhury, M. Chubarov, Y. Xiang, B. Jariwala, F. Zhang, J.M. Redwing, *Nano Lett.* **18**(2), 1049 (2018)
18. S. Tang, A. Grundmann, H. Fiadziushkin, Z. Wang, S. Hoffmann-Eifert, A. Ghiami, H. Kalisch, *Cryst. Growth Des.***23**(3), 1547 (2023)
19. M. Seol, M.H. Lee, H. Kim, K.W. Shin, Y. Cho, I. Jeon, H.J. Shin, *Adv. Mater.* **32**(42), 2003542 (2020)
20. V. Voronenkov, B. Groven, H. Medina Silva, P. Morin, S. De Gendt, *Phys. Status Solidi A* **221**(9), 2300943 (2024)
21. B. Groven, I. Kandybka, V. Voronenkov, D. Vranckx, H. Medina, S. Nijs, P. Kumar, A. Moussa, M. Saib, M. Beggiato, S. Driessen, (2024). https://doi.org/10.21203/rs.3.rs-4504047/v1
22. H. Kim, D. Ovchinnikov, D. Deiana, D. Unuchek, A. Kis, *Nano Lett.* **17**(8), 5056 (2017)
23. P. Wang, J. Lei, J. Qu, S. Cao, H. Jiang, M. He, W. Liu, *Chem. Mater.* **31**(3), 873 (2019)
24. Y. Shi, B. Groven, Q. Smets, S. Sutar, S. Banerjee, H. Medina, X. Wu, C. Huyghebaert, S. Brems, D. Lin, P. Morin, (2021, December). Superior electrostatic control in uniform monolayer MoS_2 scaled transistors via in-situ surface smoothening. In *2021 IEEE International Electron Devices Meeting (IEDM)* (pp. 37.1.1–37.1.4). IEEE.
25. T.S. Kim, K.P. Dhakal, E. Park, G. Noh, H.J. Chai, Y. Kim, K. Kang, *Small* **18**(20), 2106368 (2022)
26. K. Zhang, B.M. Bersch, F. Zhang, N.C. Briggs, S. Subramanian, K. Xu, J.A. Robinson, *ACS Appl. Mater. Interfaces* **10**(47), 40831 (2018)
27. S.H. Choi, B. Stephen, J.H. Park, J.S. Lee, S.M. Kim, W. Yang, K.K. Kim, *Sci. Rep.* **7**(1), 1983 (2017)
28. A. Cohen, A. Patsha, P.K. Mohapatra, M. Kazes, K. Ranganathan, L. Houben, A. Ismach, *ACS Nano* **15**(1), 526 (2020)
29. R.C. Rodgers, G.E. Hill, *Br. J. Anaesth.* **50**(5), 415 (1978)
30. M. Marx, A. Grundmann, Y.R. Lin, D. Andrzejewski, T. Kümmell, G. Bacher, A. Vescan, *J. Electron. Mater.* **47**, 910 (2018)
31. A. Ul-Hamid, "Contrast Formation in the SEM," in *A Beginners' Guide to Scanning Electron Microscopy*, 1st edn. (Springer, Cham, 2018), pp. 77–128
32. J.N. Kapur, P.K. Sahoo, A.K. Wong, *Comput. Vis. Graph. Image Process.* **29**(3), 273 (1985)
33. D. Reifsnyder Hickey, N. Nayir, M. Chubarov, T.H. Choudhury, S. Bachu, L. Miao, N. Alem, *Nano Lett.* **21**(15), 6487 (2021)
34. H. Ye, J. Zhou, D. Er, C.C. Price, Z. Yu, Y. Liu, J. Lowengrub, J. Lou, Z. Liu, V.B. Shenoy, *ACS Nano* **11**, 12780 (2017)
35. S.J. Liu, H. Huang, C.H. Woo, *Appl. Phys. Lett.* **80**(18), 3295 (2002)
36. Z. Chromcova, M.C. Tringides, Z. Chvoj, *J. Phys. Condens. Matter* **25**(26), 265003 (2013)
37. J.C. Kotsakidis, Q. Zhang, A.L. Vazquez de Parga, M. Currie, K. Helmerson, D.K. Gaskill, M.S. Fuhrer, *Nano Lett.* **19**(8), 5205 (2019)
38. O.M. Bunoiu, T. Duffar, I. Nicoara, *Prog. Cryst. Growth Charact. Mater.* **56**(3–4), 123 (2010)
39. S. Tang, A. Grundmann, H. Fiadziushkin, A. Ghiami, M. Heuken, A. Vescan, H. Kalisch, *MRS Adv.* **7**(30), 751 (2022)
40. T.S. Kim, G. Noh, S. Kwon, J.Y. Kim, K.P. Dhakal, S. Oh, K. Kang, *Adv. Funct. Mater.* 34(23), 2312365 (2024). https://doi.org/10.1002/adfm.202312365
41. A. Nipane, D. Karmakar, N. Kaushik, S. Karande, S. Lodha, *ACS Nano* **10**(2), 2128 (2016)
42. G. Pizzi, S. Milana, A.C. Ferrari, N. Marzari, M. Gibertini, *ACS Nano* **15**(8), 12509 (2021)
43. J. Huang, T.B. Hoang, M.H. Mikkelsen, *Sci. Rep.* **6**(1), 22414 (2016)
44. Z. Li, T. Wang, S. Miao, Z. Lian, S.F. Shi, *Nanophotonics* **9**(7), 1811 (2020)
45. J.R. Shallenberger, *Surf. Sci. Spectra* **25**, 014001 (2018). https://doi.org/10.1116/1.5016189
46. R. Addou, R.M. Wallace, *ACS Appl. Mater. Interfaces.* **8**(39), 26400 (2016)